Bespoke mirror fabrication for quantum simulation with light in open-access microcavities

BENJAMIN T. WALKER,[1,2] BENJAMIN J. ASH,[3] AURÉLIEN A. P. TRICHET,[3,4] JASON M. SMITH,[3,4] AND ROBERT A. NYMAN[1,3,*]

[1]*Quantum Optics and Laser Science group, Blackett Laboratory, Imperial College London, Prince Consort Road, SW7 2AZ, UK*
[2]*Centre for Doctoral Training in Controlled Quantum Dynamics, Imperial College London, Prince Consort Road, SW7 2AZ, UK*
[3]*Oxford HighQ Ltd, Centre for Innovation & Enterprise, Oxford University Begbroke Science Park, Begbroke Hill, Woodstock Road, Begbroke, OX5 1PF, UK*
[4]*Department of Materials, University of Oxford, Parks Road, Oxford, OX1 3PH, UK*
[*]r.nyman@imperial.ac.uk

Abstract: In this work, we use focused ion beam (FIB) milling to generate custom mirror shapes for quantum simulation in optical microcavities. In the paraxial limit, light in multimode optical microcavities follows an equation of motion which is equivalent to Schrödinger's equation, with the surface topography of the mirrors playing the role of the potential energy landscape. FIB milling allows us to engineer a wide variety of trapping potentials for microcavity light, through exquisite control over the mirror topography, including 2D box, 1D waveguide, and Mexican hat potentials. The 2D box potentials are sufficiently flat over tens of microns, that the optical modes of the cavity, found by solving Schrödinger's equation on the measured cavity topography, are standing-wave modes of the box, rather than localised to deviations. The predicted scattering loss due to surface roughness measured using atomic force microscopy is found to be 177 parts per million, which corresponds to a cavity finesse of 2.2×10^4 once other losses have been taken into account. Spectra from dye-filled microcavities formed using these features show thermalised light in flat 2D potentials close to dye resonance, and spectrally-resolved cavity modes at the predicted frequencies for elliptical potentials. These results also represent a first step towards realising superfluid light and quantum simulation in arbitrary-shaped optical microcavities using FIB milling.

1. Introduction

As quantum effects become more and more relevant for new technologies, the urgency to fully understand such effects, including emergent effects in many-body systems such as the fractional quantum Hall effect [1] and topological insulation (see [2] and references therein), increases. While classical computation has been a powerful tool for simulating new physical systems, one can derive a great advantage by embracing the idea that any system is ideally suited to simulate itself(encapsulated in the case of quantum simulation by the famous quote from Richard Feynman [3]). Simply put, we can efficiently simulate a quantum system by engineering another quantum system with an equivalent Hamiltonian.

A powerful tool for simulating wide ranges of Hamiltonians is the ability to engineer a potential energy term of our choosing. In optical microcavities, this can be done by controlling the shape of one or both of the mirrors which form the cavity. Many experiments with light in microcavities filled with fluorescent media [4–6] have exploited the fact that in the paraxial limit, a cavity

photon behaves like a massive particle moving in a potential, V, which is directly proportional to the deviation, H, of the cavity length from its longest point, L. A full description of the cavity dynamics can be derived starting from the Lugiato-Lefever equation [7] or Maxwell's equations [8]. These can be mapped in this case onto the Schrödinger-like eigenvalue equation which describes the light field in a cavity mode:

$$\frac{-\hbar^2}{2m_{ph}}\nabla^2\psi(x,y) + V(x,y)\psi(x,y) = E\psi(x,y) \tag{1}$$

to solve for the in-plane components of the cavity modes $\psi(x,y)$, or onto a complex Gross-Pitaevski equation in the presence of interactions, driving and dissipation, as shown in [8]. Here, h is Planck's constant, c^* is the speed of light in the medium, and q is the longitudinal mode number of the cavity. The effective mass m_{ph} of photons is set by the cavity cutoff wavelength λ_{cutoff} and given by $m_{ph} = h/\lambda_{cutoff}c^*$, and the potential energy term is given by

$$V(x,y) = \frac{hc^*q}{2L^2}H(x,y) \tag{2}$$

reflecting how the wavelength and therefore energy of a photon must vary with cavity length in order to match the boundary conditions imposed by the cavity mirrors.

Through manipulating $H(x,y)$, it is therefore possible to control the modes of the cavity, or equivalently in the thermodynamic limit of many thermally accessible modes the density of states (DoS), in a near arbitrary way. However, until recently the primary focus has been on parabolic potentials.

We focus in this work on open-access microcavities, which are a versatile platform for manipulating states of light. The open-access nature of the microcavities also allows the introduction of novel materials to simulate particle-particle interaction terms in the Hamiltonian, as well as allowing the resonance of the cavity to be tuned. Open-access optical microcavities have been used extensively in experiments requiring enhanced light-matter interaction [9], including atom detection [10], cavity quantum electrodynamics [11] and single-photon production and detection [12,13]. Such experiments use the Purcell effect to enhance the coupling between light and matter, and therefore stronger confinement and larger electric fields are advantageous. As a result such cavities often only have one optical mode of interest.

There are two important ingredients to engineering a Hamiltonian which may show interesting physics and therefore warrant simulation. The first is the trapping potential, which can also be used to define the topology of the system. The second is the interactions between the particles, for which the technology in photonic condensates is nascent but developing, and highly compatible with open-access microcavities. The enhanced light-matter coupling present with mode volumes of the order one wavelength cubed allows further prospects for engineering sufficiently large interactions at the few-photon level.

In addition to these two standard Hamiltonian terms, there have been recent developments in simulating more exotic terms in photonic systems. For example, Clark *et. al.* [14] use a twisted bowtie cavity to simulate the effect of a charged particle in a magnetic field, opening up even more avenues for simulating interesting Hamiltonians using photons through carefully manipulation of the optical environment.

There exist several methods for manipulating mirror shapes and therefore potentials in open-access microcavity mirrors, including CO_2 laser ablation [15], surface delamination [16–18], and greyscale lithography [19]. CO_2 laser ablation allows spherical shapes with variable radius of curvature and depth to be fabricated, but it is not trivial to extend this method to other shapes. The surface delamination technique presented in [16] allows for arbitrary shapes with a low surface roughness but is currently limited to feature depths of no more than 15 nm. FIB milling on the other hand is able to create features which are both deep (several hundreds of nanometres), and have near arbitrary shapes.

Earlier development of FIB milling for optical microcavities [20] has focused on the ability to achieve small mode volumes, which means creating features with a small radius of curvature (down to 4.3 μm in [20]) and therefore only milling a small amount of material of order 1 μm^3. Mirrors used in photon Bose-Einstein condensation experiments have milled a greater volume of material by 2 orders of magnitude [21]. These features required further smoothing using a CO_2 laser reflow technique. In this work, we present features with a further factor of three increase in volume milled which did not undergo any additional smoothing step. These features explore a much wider range of mirror topographies and, based on results in [22], give longer cavity lifetimes (10 ps) by a factor of two. This corresponds to a scattering loss of around 2600 ppm from the featured mirror and a finesse of 2.4×10^3.

We use optical microcavities formed of one planar mirror, and one sculpted mirror, and study the states of light in the cavity by filling it with a fluorescent dye (Rhodamine-6G) with broad absorption and emission cross-sections. The dye is pumped away from cavity resonance and then emits into and absorbs from the cavity modes. The featured mirror is fabricated starting from a highly polished fused silica substrate (0.3 nm root mean squared (rms) roughness), from which material is milled out using a Zeiss Crossbeam 540 FIB machine to achieve the desired shape. The featured fused silica substrate is then commercially coated with a distributed Bragg reflector, centred at 578 nm with 30 parts per million (ppm) transmission, giving an upper bound of 10^5 for the achievable finesse. This method now gives us unprecedented freedom to consider in what potential landscapes would we like to study the behaviour of thermalising light.

While we primarily consider analogue potentials in this paper, the methods presented here can also be used to engineer lattice potentials. Using lattice potentials one can for example map a wide range of computationally hard problems onto classical spin models [23]. Solving these spin models then becomes an important task for quantum simulation, which has received much interest [24–27], including in optical microcavities [28].

2. Implementation

In Fig. 1 we show the results of fabricating a wide range of potentials, including box, 1D waveguide, elliptical, spiral, Mexican hat, and ring potentials. Some of the 1D waveguides are designed with additional confining features to study coupling and transport between localised modes via the 1D channel. The transverse resolution of FIB is, in principle less than 10 nm, but we limit ourselves to 300 nm or more to ensure that no surfaces present large angles so that the dielectric coatings remain effective for the chosen wavelengths of light at notionally normal incidence. With the achievable transverse resolution, exotic structures like lattices with tunnelling anywhere from negligible (far smaller than loss rates) to infinite (indistinguishable from flat surfaces) would be achievable.

The depth of the confining potentials was chosen so as not to be a whole number of half-wavelengths of light in the cavity medium under normal working conditions, assuming a cavity cutoff wavelength of 590 nm, thereby reducing coupling between the cavity modes of interest, and the planar-planar modes in the surrounding substrate. With the additional constraint of balancing milling time with the requirement for deep confining potentials, this target depth was set at 279 nm.

The two most important characteristics of the microfabricated mirrors are how closely the milled features match the target shapes, and the lifetime of photons in the cavities they produce. We use a phase-shift interferometry to measure the former, and atomic force microscopy (AFM) measurements to estimate the latter.

The shape of the milled features is measured with a MicroXam optical profilometer which uses phase-shift interferometry to measure the profile of the milled features post-coating with a height resolution of 0.1 nm and an in-plane resolution of 0.5 μm. Figure 2 shows an example MicroXam measurement, along with a 1D slice through the data parallel to the edge of the box
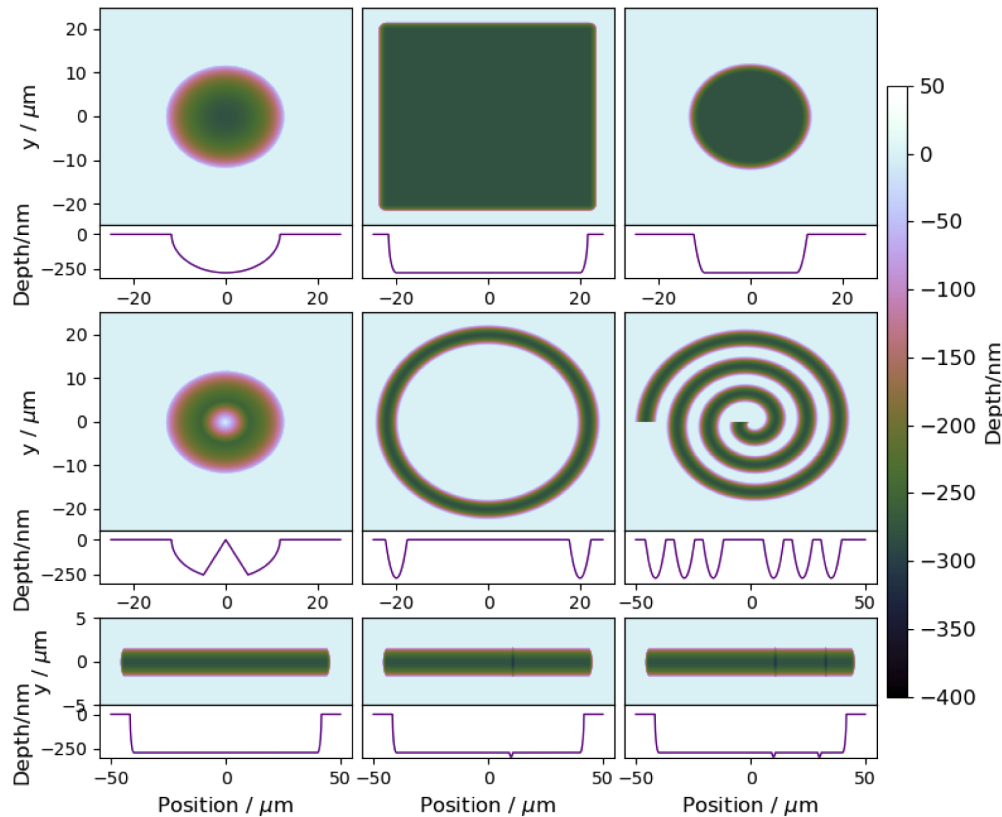
Fig. 1. Gallery of milled shapes, showing the full 2D profile, along with a 1D cut through the centre to provide more quantitative depth information. From left to right, top row: parabolic potential; square well; circular well. Middle row: Mexican hat; ring; spiral. Bottom row: 1D potential; 1D with single extra dip; 1D with two extra dips.

(interpolating within the 2D grid of MicroXam data). The fit shown in Fig. 2 uses the full 2D dataset. We chose one of the larger square box potentials to study in this section as it has the largest quantity of material milled out from it, meaning the resulting surface quality is expected to be the worst of all the features. We note that Trichet *et. al.* [20] report that FIB milling progressively smooths rough surfaces as the depth is increased, but the initial surface roughness in that work is much higher than in this.

The milled shape is around 50 nm deeper than the target shape, most likely due to a discrepancy between the set ion beam current and the true ion beam current. Therefore if a high degree of precision in absolute depth is required, careful calibration is necessary. However since the overall shape is the key feature here, this global height scaling is less important.

The inset in Fig. 2 gives a more detailed view of the roughness along the bottom of the box potential. In order to understand the impact of this small wavevector surface roughness on the cavity modes in the box potential, and in particular whether it leads to localised modes, we numerically solve Schrödinger's equation on the potential derived from MicroXam data using Eq. (2), giving the cavity modes shown in Fig. 2. With some detailed corrections, these modes are roughly the standing-wave modes of the box as required, and not localised modes.

The other effect of the surface roughness is to cause scattering loss, thereby decreasing cavity lifetime. A simple way to relate the scattering loss Λ to the surface roughness σ_{rms} is via the
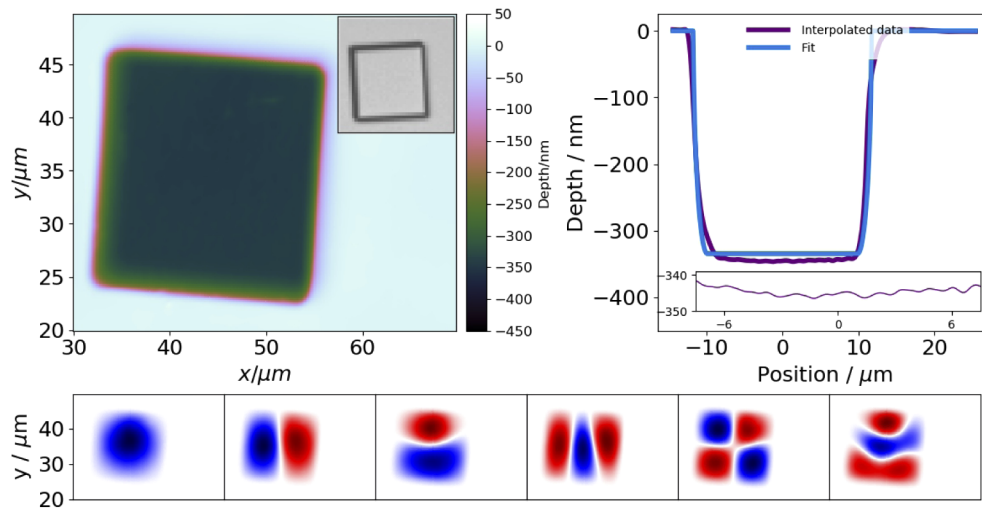
Fig. 2. MicroXam analysis of milled shape of a box potential. Top left: raw MicroXam data (Inset: example microscope image of mirror-coated feature). Top right: 1D slice through the data (tilted to be parallel to the box edges) with a fit based on the design shape and an inset showing the roughness along the bottom. Bottom row: Six lowest-energy solutions to Schrödinger's equation using the potential derived from the MicroXam data.

Debye-Waller factor:

$$\Lambda = 2\sigma_{\mathrm{rms}}{}^2 k_i^2 \tag{3}$$

where k_i is the wavevector of the incident light. This formula assumes a gaussian distribution for roughness, and would for example predict a high scattering loss for a smooth spherical mirror. A more accurate prediction of the scattering loss can be obtained by measuring the surface profile using AFM and using the power spectral density of roughness to calculate scattering loss as a function of roughness wavevector. This procedure outlined in Appendix A, based off work introduced in [29] and summarised in [30]. The Debye-Waller factor predicts a scattering loss of 515 parts per million (ppm), while the more detailed analysis predicts a scattering loss of 177ppm (with 1.4 nm r.m.s. roughness measured). The surface roughness of the unmilled substrate is 0.3 nm, corresponding to a scattering loss of 45ppm, which is found to be unaffected by any of the handling and coating procedures.

It is informative to estimate the photon-energy scales associated with the surface height. For the 10th longitudinal cavity mode with no solvent in the cavity, and a cutoff wavelength around 590 nm, 1 nm of surface height corresponds to about $k_B \times 4$ K (where k_B is the Boltzmann constant). Thus, roughness typically corresponds to a few Kelvin, whereas the features are more than 1000 K deep, which is enough to confine photon modes which are thermally excited above the cutoff energy.

3. Cavity spectra

The microfabricated mirrors are used with an opposing planar mirror ≈ 1 μm away to form an optical microcavity which is filled with a 2 mM solution of Rhodamine-6G dye as in photon Bose-Einstein condensation experiments [4–6], and pumped using a 532 nm laser to achieve a thermal population of the cavity modes. Figure 3 shows the output spectra for a 40 μm box potential with a cavity detuning close to dye resonance (left panel) showing good thermalisation, and far from dye resonance (right panel) showing poor thermalisation. The theory fit is made up of the discrete standing-wave modes of the 2D box, populated according to a Bose-Einstein

distribution, and broadened to reflect the resolution of the spectrometer. With little or no spectral redistribution of the light by the thermalising dye medium (right panel), we expect a spectrum which more closely matches the flat density of states of the box potential, as demonstrated. This presence of thermalised light in a 2D box potential will allow future experiments to measure the presence or absence of superfluid behaviour in such systems.
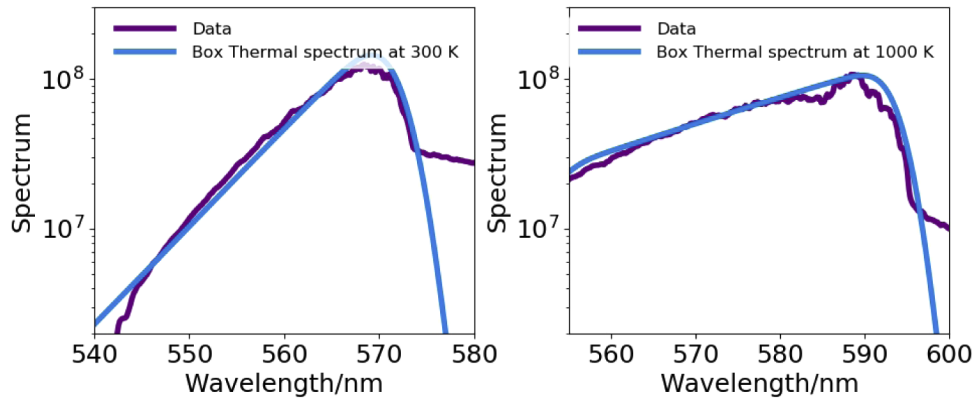
Fig. 3. Cavity output spectrum with a 40 μm FIB-milled box potential showing good thermalisation to the predicted spectrum at short cutoff wavelength, close to dye resonance (left panel) and poor thermalisation more closely matching the flat density of states for a 2D box potential at long cutoff wavelengths, far from dye resonance (right panel). The spacing between the 2D box modes is of order 50 pm and is therefore not resolved by the current imaging optics.

Figure 4 shows the cavity output spectrum from an elliptical feature with radius of curvature (RoC) 500 μm in one direction and 180 μm in the other. The vertical lines show the predicted wavelengths of the eight lowest-energy modes, given the cavity cutoff and the longitudinal mode number of 10, all of which match the spectrum and, crucially, can be spectrally resolved. Previous
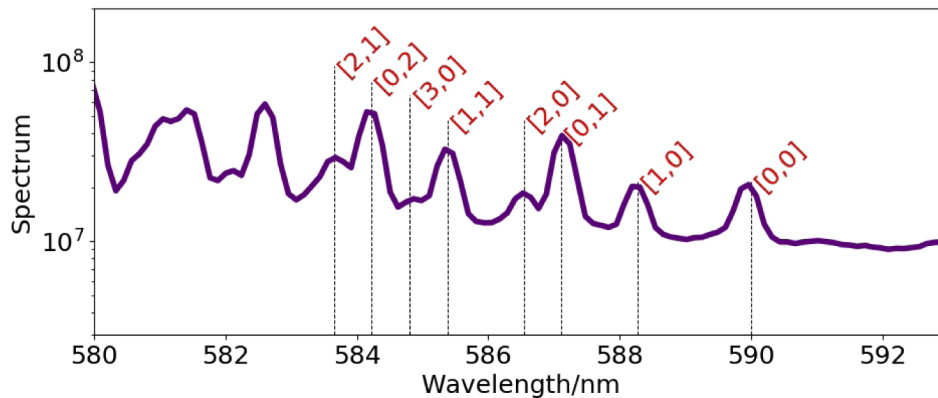
Fig. 4. Cavity output spectrum for an elliptical potential, with vertical lines showing the expected locations of peaks from the eight lowest-energy modes of the cavity based on mirror radii of curvature 500 μm and 180 μm. Red text [i,j] labels the number of excitations i and j along the 500 μm and 180 μm RoC directions respectively. The linewidths of the peaks in this spectrum are expected to be limited by the imaging optics and not reflect the true linewidths of the cavity modes. The cavity cutoff wavelength is 590 nm, corresponding to the partial thermalisation of the light.

theoretical [31,32] and experimental [21,22] work has studied the effect of the spatial distribution of cavity modes on the phenomenon of multimode condensation. This breaking of the degeneracy of the excited modes in a two-dimensional harmonic system will allow new experimental insights into such effects.

Spherical microcavity mirrors fabricated in the same batch as those presented in this paper have been used to achieve Bose-Einstein and multimode photon condensation [22]. The degree of thermalisation achieved in these experiments implies roughly a factor of two increase in cavity lifetime from 5.2 ps to 10.4 ps with these features compared to previous features [21], implying a true cavity finesse of 2.5×10^3, and an average scattering loss of 1250 ppm at each mirror.

4. Conclusion

We have used focused ion beam milling to engineer optical microcavities with custom trapping potentials for light. Phase-shift interferometry measurements of the milled shapes after mirror coating predict good agreement with the target cavity modes for flat box potentials, despite the three-fold increase in volume of material milled relative to previous work [21], and the absence of any additional smoothing steps. Dye-filled optical microcavity measurements demonstrate thermalised light in a flat 2D potential, giving prospects for measuring superfluid behaviour of light.

The control over the cavity modes demonstrated by the elliptical cavities opens doors for quantum simulation with tuneable coupling between optical modes, as well as having benefits for current research into the spatial dynamics in photon condensate experiments. The Mexican hat potentials presented here demonstrate the ability to engineer topologically non-trivial systems. Further possibilities for future experiments include measuring Anderson localisation using random potentials in dye-filled optical microcavities, and fabricating non-planar ring resonators.

Appendix A. Calculating scattering loss from surface topography

To a first approximation, the scattering loss (Λ) from a rough surface is given by the Debye-Waller factor

$$\Lambda = 2\sigma_{\text{rms}}{}^2 k_{\text{i}}^2 \tag{4}$$

where σ_{rms} is the root mean squared surface roughness, and k_{i} is the wavevector of the incident light. The root mean squared roughness for the bare substrate and the 40 μm milled box are 0.3 nm and 1 nm implying scattering losses of 45 ppm and 230 ppm, and limiting finesses to 2.3×10^4.

The Debye-Waller factor however does not take into account how the in-plane wavevector of the surface roughness affects the amount of scattering loss. If the roughness is all on a lengthscale much shorter than the wavelength of the incident light, then the incident light is not able to probe this roughness, and it does not cause significant scattering loss. If the lengthscale of the surface roughness is large compared to the wavelength of the incident light, this 'roughness' appears as a global shaping of the mirror, and good reflection is still achieved. These two effects are quantified in [30] which starts from Maxwell's equations to derive an expression in Eq. (5) for the total scattering loss as a function of surface profile, $h(x, y)$. θ_2 and θ_3 are the angles between the scattered light and the incident light (assumed normal), and the x direction respectively, and k is the wavevector of the incident light. The derivations in [30] are based off earlier work in a book by Ogilvy [29].

$$\Lambda = \int_{\theta_3=0}^{2\pi} \int_{\theta_2=0}^{\pi/2} 4k^4 \cos^2\theta_2 \sin\theta_2 P(kA, kB) \mathrm{d}\theta_2 \, \mathrm{d}\theta_3 \tag{5}$$

$$\text{with } A = -\sin\theta_2 \cos\theta_3 \text{ and } B = -\sin\theta_2 \sin\theta_3$$

$$P(k_x, k_y) = \lim_{A_M \to \infty} \frac{1}{4\pi^2 A_M} \left| \int h(x, y) \, e^{i(k_x x + k_y y)} \, dx \, dy \right|^2 \tag{6}$$

$P(k_x, k_y)$ is simply the power noise spectrum of the surface roughness which can be calculated easily from the surface profile using python (or most other languages), before using a Jacobian transformation to cast Eqn. (5) as an integral over k_x and k_y.

Figure 5 shows the surface profile of the milled substrate after mirror coating, as measured by AFM (left), along with the power noise spectrum of the roughness (middle) and amount of scattering loss as a function of the two in-plane wavevectors of roughness. Figure 6 shows the same analysis for the 40 μm box potential. We can see that the majority of the contribution to the total scattering loss comes from wavevectors of roughness between $k/2$ and k. The scattering loss figures presented in the main text are the integrals of the right-hand panels in Figs. 5 and 6.
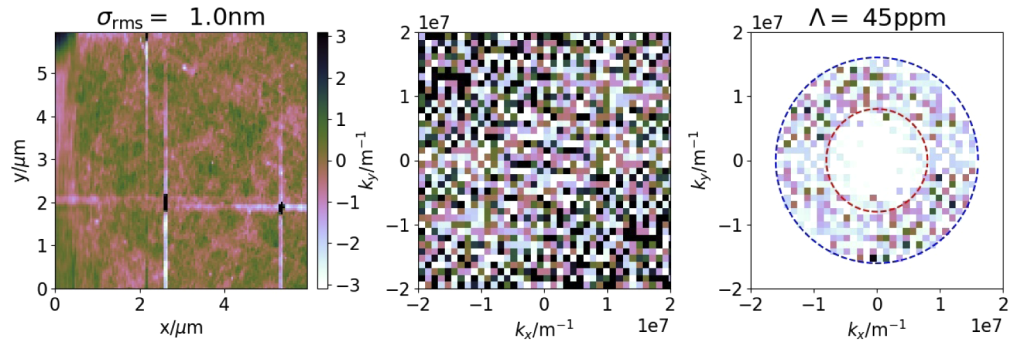
Fig. 5. Left: AFM surface profile of an unmilled portion of substrate which has gone through all the same handling and coating procedures as the milled features. Middle: Power noise spectrum of surface roughness. The colourbar represents height in nm. Right: Calculated loss as a function of in-plane roughness wavevector.
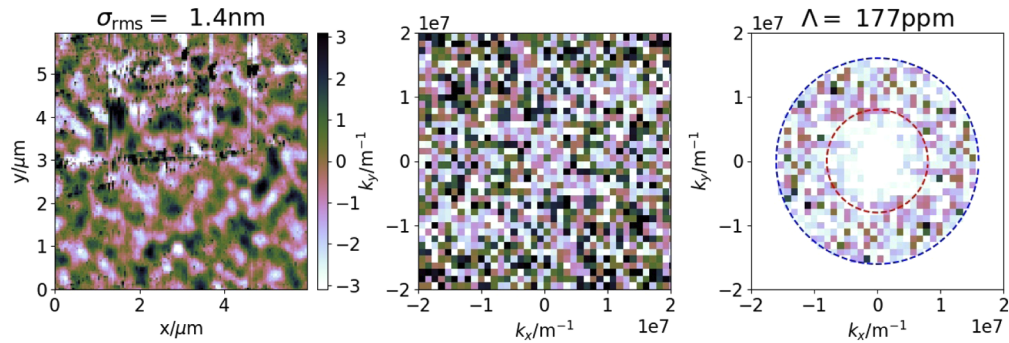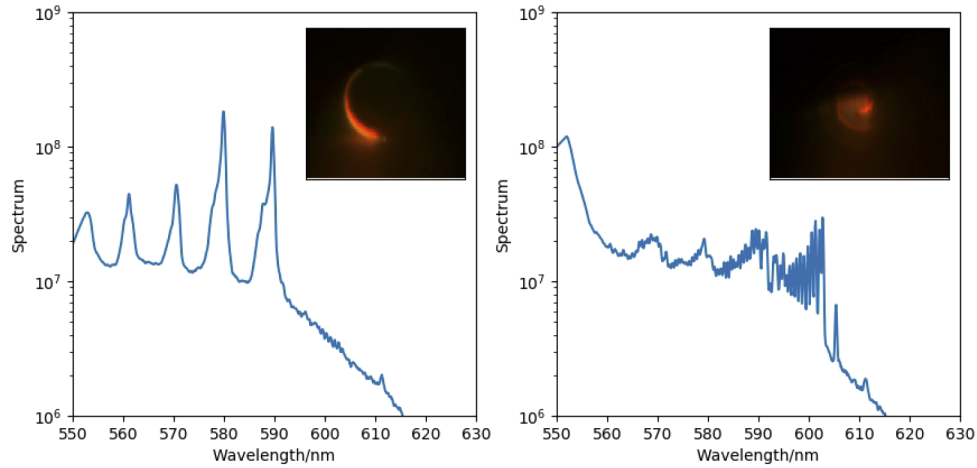

Fig. 6. Left: AFM surface profile of the bottom of a 40 μm box potential. The colourbar represents height in nm. Middle: Power noise spectrum of surface roughness. Right: Calculated loss as a function of in-plane roughness wavevector.

Appendix B. Other cavity spectra and images

Some additional spectra and camera images of cavity output light are shown in Figs. 7 and 8.

Fig. 7. Spectra and camera images (insets) of cavity output light for a spiral potential pumped with a focused pump spot on the outer end (left) and inner end (right). Both spectra shows manifolds spaced by roughly 10 nm due to excitations in the direction transverse to the spiral. When the pump is in the centre where the curvature of the spiral is tighter, the spectrum also resolves modes along the direction of the spiral. In both cases, the camera image gives some indication of how well light is transported along the spiral.
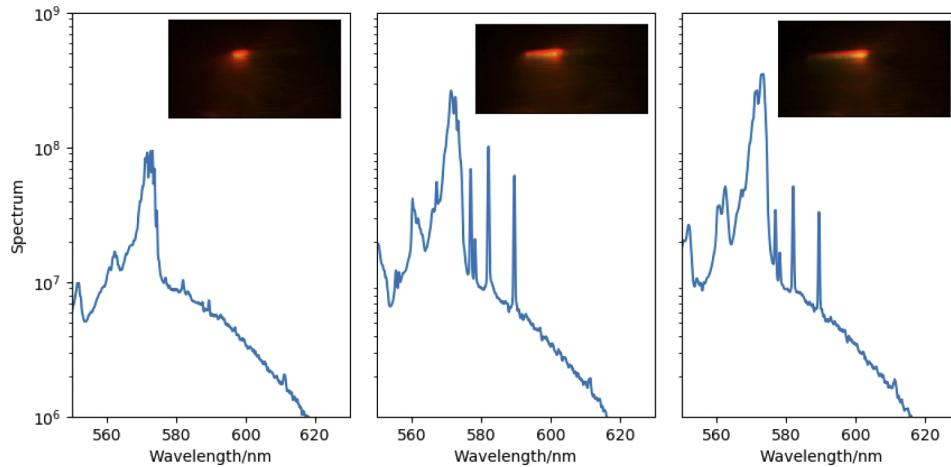
Fig. 8. Spectra and camera images (insets) of cavity output light from an $80\ \mu$m 1D waveguide with an additional 60 nm dip in the centre, pumped with a focused pump spot on the left, middle and right respectively. The right two panels show the bound modes at longer wavelengths as well as the quasi-continuum of the waveguide at shorter wavelengths. The absence of the peaks from the tightly bounds in the left spectrum suggests that transport preferentially occurs from right to left, possibly due to the 45 degree angle of the pump beam.

Data availability. Data underlying the results presented in this paper are not publicly available at this time but may be obtained from the authors upon reasonable request.

References

1. D. C. Tsui, H. L. Stormer, and A. C. Gossard, "Two-dimensional magnetotransport in the extreme quantum limit," Phys. Rev. Lett. **48**(22), 1559–1562 (1982).
2. M. Z. Hasan and C. L. Kane, "Colloquium: topological insulators," Rev. Mod. Phys. **82**(4), 3045–3067 (2010).
3. R. P. Feynman, "Simulating physics with computers," Int. J. Theor. Phys. **21**(6-7), 467–488 (1982).
4. J. Klaers, J. Schmitt, F. Vewinger, and M. Weitz, "Bose-einstein condensation of photons in an optical microcavity," Nature **468**(7323), 545–548 (2010).
5. J. Marelic and R. A. Nyman, "Experimental evidence for inhomogeneous pumping and energy-dependent effects in photon bose-einstein condensation," Phys. Rev. A **91**(3), 033813 (2015).
6. S. Greveling, K. Perrier, and D. van Oosten, "Density distribution of a bose-einstein condensate of photons in a dye-filled microcavity," Phys. Rev. A **98**(1), 013810 (2018).
7. L. A. Lugiato and R. Lefever, "Spatial dissipative structures in passive optical systems," Phys. Rev. Lett. **58**(21), 2209–2211 (1987).
8. R. Nyman and M. Szymańska, "Interactions in dye-microcavity photon condensates and the prospects for their observation," Phys. Rev. A **89**(3), 033844 (2014).
9. S. Johnson, P. Dolan, T. Grange, A. Trichet, G. Hornecker, Y.-C. Chen, L. Weng, G. Hughes, A. Auffeves, and J. Smith, "Tunable cavity coupling of the zero phonon line of a nitrogen-vacancy defect in diamond," arXiv preprint arXiv:1506.05161 (2015).
10. M. Trupke, J. Goldwin, B. Darquié, G. Dutier, S. Eriksson, J. Ashmore, and E. Hinds, "Atom detection and photon production in a scalable, open, optical microcavity," Phys. Rev. Lett. **99**(6), 063601 (2007).
11. Y. Colombe, T. Steinmetz, G. Dubois, F. Linke, D. Hunger, and J. Reichel, "Strong atom–field coupling for bose–einstein condensates in an optical cavity on a chip," Nature **450**(7167), 272–276 (2007).
12. A. Jeantet, Y. Chassagneux, C. Raynaud, P. Roussignol, J.-S. Lauret, B. Besga, J. Estève, J. Reichel, and C. Voisin, "Widely tunable single-photon source from a carbon nanotube in the purcell regime," Phys. Rev. Lett. **116**(24), 247402 (2016).
13. P. Dolan, S. Adekanye, A. Trichet, S. Johnson, L. Flatten, Y. Chen, L. Weng, D. Hunger, H.-C. Chang, S. Castelletto, and J. M. Smith, "Robust, tunable, and high purity triggered single photon source at room temperature using a nitrogen-vacancy defect in diamond in an open microcavity," Opt. Express **26**(6), 7056–7065 (2018).
14. L. W. Clark, N. Schine, C. Baum, N. Jia, and J. Simon, "Observation of laughlin states made of light," Nature **582**(7810), 41–45 (2020).
15. D. Hunger, C. Deutsch, R. J. Barbour, R. J. Warburton, and J. Reichel, "Laser micro-fabrication of concave, low-roughness features in silica," AIP Adv. **2**(1), 012119 (2012).
16. C. Kurtscheid, D. Dung, E. Busley, F. Vewinger, A. Rosch, and M. Weitz, "Thermally condensing photons into a coherently split state of light," Science **366**(6467), 894–897 (2019).
17. C. Kurtscheid, D. Dung, A. Redmann, E. Busley, J. Klaers, F. Vewinger, J. Schmitt, and M. Weitz, "Realizing arbitrary trapping potentials for light via direct laser writing of mirror surface profiles," Europhys. Lett. **130**(5), 54001 (2020).
18. E. Epp, N. Ponnampalam, W. Newman, B. Drobot, J. McMullin, A. Meldrum, and R. DeCorby, "Hollow bragg waveguides fabricated by controlled buckling of si/sio 2 multilayers," Opt. Express **18**(24), 24917–24925 (2010).
19. N. Lassaline, R. Brechbühler, S. J. Vonk, K. Ridderbeek, M. Spieser, S. Bisig, B. le Feber, F. T. Rabouw, and D. J. Norris, "Optical fourier surfaces," Nature **582**(7813), 506–510 (2020).
20. A. A. Trichet, P. R. Dolan, D. M. Coles, G. M. Hughes, and J. M. Smith, "Topographic control of open-access microcavities at the nanometer scale," Opt. Express **23**(13), 17205–17216 (2015).
21. B. T. Walker, L. C. Flatten, H. J. Hesten, F. Mintert, D. Hunger, A. A. P. Trichet, J. M. Smith, and R. A. Nyman, "Driven-dissipative non-equilibrium bose–einstein condensation of less than ten photons," Nat. Phys. **14**(12), 1173–1177 (2018).
22. J. D. Rodrigues, H. S. Dhar, B. T. Walker, J. M. Smith, R. F. Oulton, F. Mintert, and R. A. Nyman, "Unsupervised learning of the fuzzy phases of small photonic condensates," arXiv preprint arXiv:2006.12298 (2020).
23. G. De las Cuevas and T. S. Cubitt, "Simple universal models capture all classical spin physics," Science **351**(6278), 1180–1183 (2016).
24. K. Kim, M.-S. Chang, S. Korenblit, R. Islam, E. E. Edwards, J. K. Freericks, G.-D. Lin, L.-M. Duan, and C. Monroe, "Quantum simulation of frustrated ising spins with trapped ions," Nature **465**(7298), 590–593 (2010).
25. J. Simon, W. S. Bakr, R. Ma, M. E. Tai, P. M. Preiss, and M. Greiner, "Quantum simulation of antiferromagnetic spin chains in an optical lattice," Nature **472**(7343), 307–312 (2011).
26. J. Struck, C. Ölschläger, R. Le Targat, P. Soltan-Panahi, A. Eckardt, M. Lewenstein, P. Windpassinger, and K. Sengstock, "Quantum simulation of frustrated classical magnetism in triangular optical lattices," Science **333**(6045), 996–999 (2011).

27. Y. Salathé, M. Mondal, M. Oppliger, J. Heinsoo, P. Kurpiers, A. Potočnik, A. Mezzacapo, U. Las Heras, L. Lamata, E. Solano, S. Filipp, and A. Wallraff, "Digital quantum simulation of spin models with circuit quantum electrodynamics," Phys. Rev. X **5**(2), 021027 (2015).
28. N. G. Berloff, M. Silva, K. Kalinin, A. Askitopoulos, J. D. Töpfer, P. Cilibrizzi, W. Langbein, and P. G. Lagoudakis, "Realizing the classical xy hamiltonian in polariton simulators," Nat. Mater. **16**(11), 1120–1126 (2017).
29. J. A. Ogilvy and H. M. Merklinger, "Theory of wave scattering from random rough surfaces," (1991).
30. R. Nyman and B. Walker, "Wave scattering from rough surfaces for good mirrors," arXiv preprint arXiv:2005.05201 (2020).
31. H. J. Hesten, R. A. Nyman, and F. Mintert, "Decondensation in nonequilibrium photonic condensates: When less is more," Phys. Rev. Lett. **120**(4), 040601 (2018).
32. B. T. Walker, H. J. Hesten, H. S. Dhar, R. A. Nyman, and F. Mintert, "Noncritical slowing down of photonic condensation," Phys. Rev. Lett. **123**(20), 203602 (2019).